Nanoscale

Strain in Single-Wrinkle on MoS_2 Flake for in-Plane Realignment of Band-Structure for Enhanced Photo-Response

Journal:	*Nanoscale*
Manuscript ID	NR-ART-07-2018-005884.R3
Article Type:	Paper
Date Submitted by the Author:	23-Nov-2018
Complete List of Authors:	Deng, Shikai; University of Illinois at Chicago, Chemical Engineering Che, Songwei; University of Illinois at Chicago, Chemical Engineering Debbarma, Rousan; University of Illinois at Chicago, Chemical Engineering Berry, Vikas; University of Illinois at Chicago, Department of Chemical Engineering

Strain in Single-Wrinkle on MoS_2-Flake for in-Plane Realignment of Band-Structure for Enhanced Photo-Response

*Shikai Deng, Songwei Che, Rousan Debbarma and Vikas Berry**

Department of Chemical Engineering, University of Illinois at Chicago, 810 South Clinton Street, Chicago, Illinois 60607, United States

*E-mail: vikasb@uic.edu

ABSTRACT

Since 2D transition metal dichalcogenides (TMDs) exhibit strain-tunable bandgap, locally confining strain can allow lateral manipulation of band-structure, in-plane carrier transport and optical transitions. Here we show that a single wrinkle (width = 10 nm ~ 10 μm) on MoS_2 flake can induce confined uniaxial strain to reduce local bandgap (40~60 meV/% deformation) producing a microscopic exciton funnel with an enhancement in photocurrent over flat MoS_2 devices. The study also shows that wrinkle can spatially reconfigure distribution of doping and enhance light absorption in MoS_2 layer by Fabry-Perot interference of nanocavity. In field-effect transistor studies on MoS_2 flat-wrinkle-flat device-structure, a higher carrier mobility and an improvement in the on/off ratio are exhibited in the devices with a single wrinkle. This phenomenon is attributed to the built-in potential induced by bandgap-reduction at the wrinkle site and the change in doping of the suspended wrinkle. The wrinkle-induced tunability of local bandgap and manipulation of spatial transport barriers and light absorption can evolve electronics and optoelectronic guided by in-plane deformation of single 2D nanomaterial.

Keywords: MoS_2; wrinkles; strain; doping variation; in-plane transport, photosensitivity

Introduction

The properties of materials can be tuned over a wide range *via* strain engineering by altering their mechanical or structural attributes. However, challenge with creation of local strain at micron scale and the low failure strains (~0.1%) of bulk crystalline materials limit the extent to which their properties can be modified mechanically. Atomically thin two-dimensional nanomaterials (2DNMs) are particularly well-suited for strain engineering because they can withstand a larger strain (e.g. up to 25% for graphene and 11% for MoS_2) before rupturing;[1–5] and wrinkles in 2DNMs induce confined, uniaxial strain dependent on the wrinkle-attributes (orientation, size, shape, and number). Further, wrinkling of 2DNMs leads to delamination and separation from the substrate creating a gradient (variation) in doping (from substrate or adsorbed molecules), which can further modify carrier-transport properties.

Wrinkles in 2DNMs[6–8] can form naturally *via* thermal vibrations (internal ripples)[9–11] and edge instabilities;[12] while wrinkles can be induced *via* flexible substrate deformation,[5,13–15] pre-strained substrate-relaxation,[7,16,17] high solvent-surface-tension during transfer,[18] and thermal expansion mismatch between 2DNMs and the substrate during chemical vapor deposition (CVD).[19,20] The local strain governed by the physical attributes of the wrinkles[21] influences the electronic structure,[22,23] local charge distribution,[24] dipole moment,[25] optical properties;[7,16] and the local chemical potential of the 2DNMs.[26] The presence of a bandgap in some TMDs opens the possibility of efficient photonic applications. MoS_2 transistors exhibit high on/off ratios[27] and high photoresponsivity.[28] Here, we demonstrate that a single wrinkle on MoS_2 flake (produced via mechanical exfoliation on SiO_2 substrates) can enable local manipulation of the lateral electron band structure, regulation of the in-plane carrier transport and enhancement of the optoelectronic response. Moreover, the geometric shapes of the wrinkles (symmetric, asymmetric, and folded) affect the magnitude of strain, and in turn, influence the properties of MoS_2 as confirmed by Raman and photoluminescence spectra.

Results & discussion

Samples of wrinkled MoS_2 flakes on SiO_2 substrates were identified after exfoliation (one in ten sheets had wrinkles), as shown in Figure 1a and Figure S1, S2. Although, there is little control on producing wrinkles, the adhesion between MoS_2 and the SiO_2 substrate appears to have an influence on wrinkle formation during the exfoliation process.[29] An optimal rate of release of the tape is important to increase the probability of wrinkle formation (faster release leads to smaller flakes; while slower release causes lesser wrinkles), where a partial delamination of MoS_2 from the substrate leads to the bending and wrinkling of MoS_2. The structure of the wrinkle is governed by the interplay between the interfacial adhesion of SiO_2 with MoS_2, and the bending energy of the

MoS_2 flake. It is important to note that the adhesive tape (Scotch tape) retains the unpeeled MoS_2 and therefore has no contact with the peeled MoS_2 flake. Therefore, there is no residue from the tape that can induce electrostatic charging at the surface of MoS_2 flakes (see the Experimental and Methods section for details).

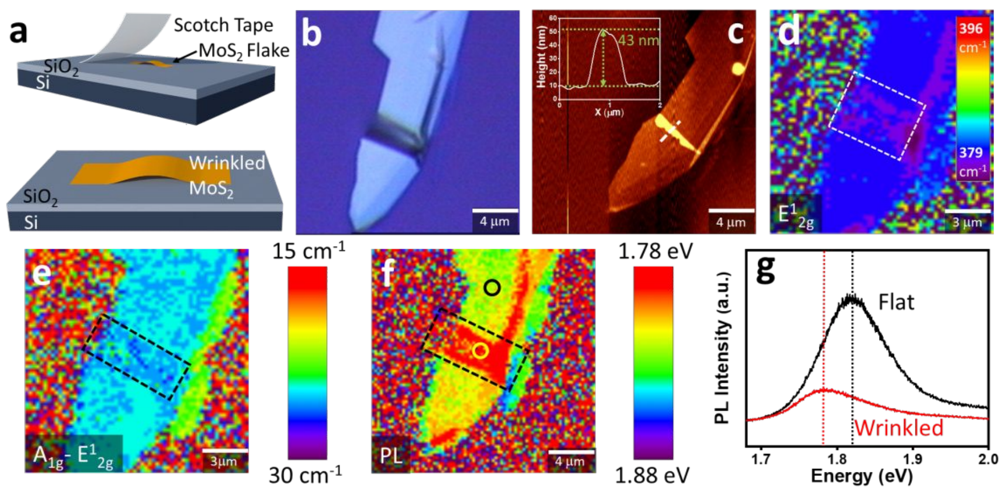

Figure 1. Single wrinkle in MoS_2 on SiO_2. (a) Schematic of wrinkled MoS_2 on SiO_2 substrate. (b) Typical optical image of a wrinkled MoS_2. (c) Atomic force microscopy characterization image of the wrinkled part of MoS_2 in (b), The inset is the height profile of the dashed line in (c). (d) Raman position mapping of E^1_{2g} mode. (e) Raman position difference between E^1_{2g} mode and A_{1g} mode (A_{1g} - E^1_{2g}). (f) Photoluminescence (PL) energy mappings of A exciton peak. (g) PL spectra profiles measured on a flat (black) and on a wrinkled (yellow) region.

A typical wrinkled MoS_2 film on SiO_2 as observed under an optical microscope is shown in Figure 1b. Three-dimensional profiles of wrinkles in MoS_2 obtained via atomic force microscope (AFM) is shown in Figure 1c and Figure S3. Both the height of the wrinkle (~43 nm with a width of ~0.8 μm) and the thickness of this MoS_2 film (~10 nm) were measured for the typical wrinkled shown in Figure 1b. Interestingly, in most cases, the wrinkles were stable and the sheets did not slip on the SiO_2 surface. This is attributed to the relatively strong interfacial adhesion between MoS_2 and SiO_2 surface. However, in some cases with smaller flakes, the wrinkles flattened over time due to MoS_2 slipping (see supplementary information Figure S4). It is important to note that this slipping/sliding is usually caused by a lateral force from the uniaxial strain from bends and bend-like-geometries in atomically thin 2D crystals (e.g. graphene, MoS_2).

The structural attributes of the wrinkles can be used to calculate the adhesion energies (γ) (between MoS_2 and its supporting substrates) and deformation ($\Delta = \frac{L_0 - L_p}{L_0}$) *via* force and energy balance:[29]

$$\gamma = \frac{\pi^4 E t^3 A^2}{6\lambda^4} \quad (1)$$

$$\Delta = \frac{3\gamma\lambda^3}{2\pi^2 E t^3 L_p} \quad (2)$$

where E is the Young's modulus of MoS_2, A is the amplitude and λ is the width of the wrinkle, t is the thickness of the thin film, and L_0 and L_p are the length and projected length of the wrinkled MoS_2 on substrates, respectively. The height of the wrinkle is not required in the deformation calculation. The stability of wrinkle is determined by the bending energy in the flake and adhesion energy at interface of the MoS_2 flake and the substrate. Therefore, a flake with a deformation (Δ), it can support wrinkle with critical width λ_c. Wrinkles with width smaller than λ_c will be stable on the substrate. Wrinkles with thickness greater than 15 nm are stable, no changes were observed after one year or after the electrical device fabrication process. However, when we washed samples with acetone and isopropyl alcohol to reduce the surface adhesion, some wrinkles were flattened.

A wrinkle in MoS_2 induces modification of the strain in its atomic structure, leading to a considerable change in the lattice-vibration (phonon frequency shift). In the wrinkled region, the two most prominent Raman peaks, E^1_{2g} mode (~384 cm^{-1}) and A_{1g} mode (~405 cm^{-1}), are red-shifted (vibrations softening) compared to the flat (non-wrinkled) region as shown in Figure 1d and S3d. The A_{1g} mode (corresponding to the sulfur atoms' out-of-plane, antiphase oscillation) is less sensitive to wrinkling than the E^1_{2g} (sulfur and molybdenum atoms' antiphase oscillation parallel to the crystal plane). Both theoretical and experimental results show that the shift in the Raman peaks linearly depends on the applied strain,[7,13,30,31] therefore, the local strain in the wrinkle can be quantified through Raman spectra. The shift of E^1_{2g} peak position for this wrinkle is ~ 1.1 cm^{-1} as shown in Figure 1d. Plugging this into the relationship between strain and peak position shift,[7,13,31] the estimated deformation is ~ 0.55 %. This is consistent with the deformation obtained from the Equation 2 (also ~0.55%).

Three different geometric shapes of wrinkles were observed: symmetric (> 30 samples), asymmetric (> 10 samples) and folded (> 3 samples), as depicted in Figure 1b and S5. Although most samples were symmetric wrinkles, it is challenging to controllably form a defined shape of a wrinkle by this method. Asymmetric and folded wrinkles were typically observed in thinner flakes, attributed to reduced stiffness, increased instability and inclined peeling force. The smaller values of A_{1g} - E^1_{2g} indicate that there is lesser strain in the asymmetrical and folded MoS_2 wrinkles, comparing with symmetric wrinkles (Figure 1e and S6). Moreover, a part of the bending energy is compensated by the sharp peak in the asymmetrical regions. Further, Raman peaks do not change on the small wrinkles on the relatively thick MoS_2 flakes as shown in Figure S7 and S8, due to slight strain effects introduced by the small wrinkles.

Although multilayer MoS_2 is an indirect bandgap semiconductor, its photoluminescence spectrum is dominated by the direct gap transitions, at the K point of the Brillouin zone, between the valence band (which is split by interlayer spin−orbit coupling) and the conduction band. The indirect bandgap transition originating from hot luminescence (part of energy consumed by phonon vibration for momentum conservation)[32] only contributes to a very weak photoluminescence peak.[33] A pronounced redshift of A-exciton peak in the wrinkled region exists for a symmetric wrinkles in comparison to that of the flat region in the same flake as shown in Figure 1f and S9. This indicates that the uniaxial strain modifies the optical band structure around the K point, reducing the energy of the direct bandgap transition.[30] The red shift of the A-exciton peak for symmetric wrinkles is much larger than that for the asymmetric and folded wrinkles, as shown in Figures 1f, S6, S9 and S10, consistent with a previous study[7] on a decrease in direct bandgap (40~60 meV/% deformation) with an increase in strain (see supplementary information for more details, Table S1 and Figure S11). Here, the PL peak position of A exciton is thickness-insensitive, since K points are primarily composed of strongly localized d orbitals of Mo atom sites.[32] width

It should be pointed out that the shape-induced dissimilar modifications of Raman spectra and the photoluminescence response of MoS_2 wrinkles implies that the phonon softening and optical bandgap reduction is dominated by the strain instead of surface doping of MoS_2. If the doping variation in MoS_2 (due to partial separation from the substrate) was a predominant cause for Raman and PL shifts, the symmetric and asymmetric samples should have behaved similarly (there is no surface-induced doping in the wrinkled regions for either shapes of wrinkles). A blue shift of A-exciton is observed in the wrinkled region, since there is lesser n-doping on the wrinkled region compared to the flat region, as shown later.[34] Note that the intensity of photoluminescence in the wrinkled regions is lower than that on the flat regions, since the focal plane of the excitation laser was on the flat MoS_2 surfaces (the wrinkles were out-of-focus) and because of less light returns to the detector from the edge of wrinkles. Further, the bandgap determined by photoluminescence-spectroscopy differs from that determined by the electrical transport due to the additional exciton binding energy. Recent theoretical studies have estimated that the exciton binding energy is strain-insensitive and is of the order of 100 meV; therefore, the magnitude of transport bandgap is also expected to be reduced with strain.[35,36]

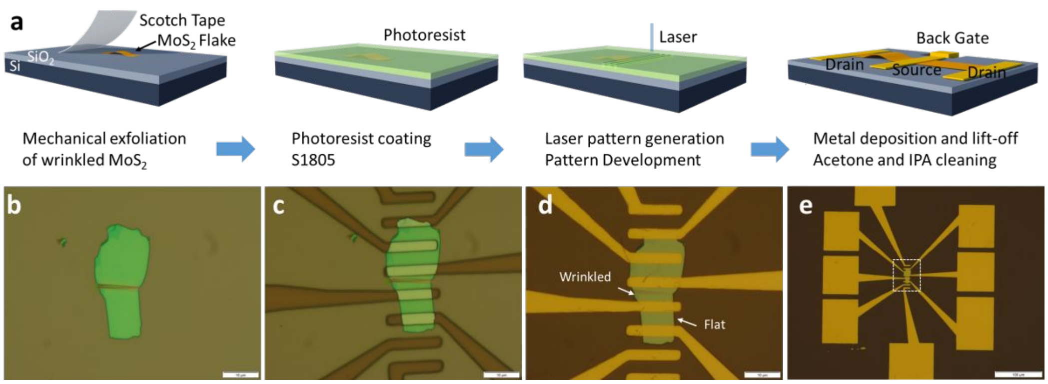

Figure 2. Device fabrication and characterization. Schematic illustration (a) and optical images (b to e) of the single-wrinkle and flat MoS_2 device fabrication process. The scale bars are 50 μm.

To study the effect of a single MoS_2 wrinkle on the in-plane charge-carrier transport, we deposited electrodes across both wrinkled and non-wrinkled (flat) regions of the same MoS_2 flake to produce field-effect transistors (Figure 3). Characterization of more devices and characterization on different flakes are shown in supplementary information. Only symmetric wrinkles were studied in these devices, since the asymmetric and/or folded wrinkles exhibited relatively smaller changes in the bandgap with strain. The wrinkles are oriented in the transverse direction to the current flow (current flowing across the wrinkle). There is an increase of barrier for the in-plane carrier-flow across the MoS_2 wrinkle as shown in supplementary information. The electrode-MoS_2 junctions are similar for both the wrinkled and flat devices, since the electrode-MoS_2 junctions are on flat MoS_2 and more than 1 μm away from the wrinkled region. Moreover, the barrier is minimally affected by contact resistance, which is much smaller than the channel resistance.[37] The higher barrier across the wrinkle is attributed to the local carrier-redistribution due to the surface charge redistribution induced by the built-in potential between wrinkle and flat region, as shown later.

The field-effect mobility of these MoS_2 devices can be measured from equations:[28,38,39]

Flat device:
$$\mu = \frac{L}{W\left(\frac{\varepsilon_r \varepsilon_0}{D}\right) V_{DS}} \frac{dI_{DS}}{dV_{BG}} \tag{3}$$

Wrinkled device:

$$\mu = \frac{L}{V_{DS}\frac{2\pi\varepsilon_r\varepsilon_0}{cosh^{-1}(\frac{r+h}{r})}}\frac{dI_{DS}}{dV_{BG}} \quad (4)$$

where, L and W are the length and width of MoS_2 channel, respectively; ε_r is relative permittivity and ε_0 is vacuum permittivity, D is the gate-oxide thickness, r is the wrinkles radius (25 nm), h is the SiO_2 thickness (285 nm). The mobility in wrinkled part of MoS_2 (estimated in a cylinder on a conducting plate model ($\mu_W = 5.55\ \mathrm{cm^2V^{-1}S^{-1}}$) is 3.9 times of the values of flat-MoS_2 devices ($\mu_F = 1.42\ \mathrm{cm^2V^{-1}S^{-1}}$) (at 30K with $V_{DS} = 1V$ and $V_{BG} = 0V$) (Table S4 and See the detailed calculation in supplementary information). The higher mobility in the wrinkled MoS_2 could be due to the suppression of electron-phonon coupling by the tensile strain (lower lattice scattering) and the low doping concentration (reducing impurities scattering) in the single-wrinkle region.[40,41]

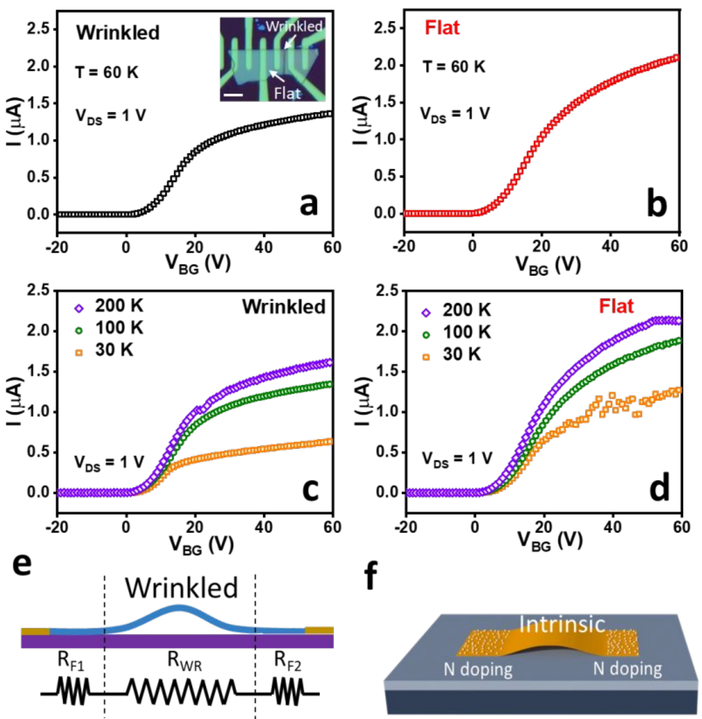

Figure 3. I_{DS}-V_{BG} (source-drain current versus back gating voltage) characterization and temperature studies of single-wrinkle and flat MoS_2 devices. (a) and (b) I_{DS} versus V_{BG} at 60K for wrinkled and flat MoS_2 devices, respectively. Inset shows the optical image of tested device and the scale bar is 10 μm. (c) and (d) I_{DS} in linear scale versus V_{BG} at different temperatures for wrinkled and flat MoS_2 devices, respectively. (e) Side-view schematic of wrinkled MoS_2 device showing the wrinkled MoS_2 resistor (R_{WR}) and two flat MoS_2 resistors in series (R_{F1} and R_{F2}). (f) Schematic illustration of wrinkled MoS_2 with n-doped (white spheres) flat parts, and intrinsic suspended wrinkled part.

Thin MoS_2 flakes in contact with SiO_2 are reported to be electron-doped (n-doped).[42] This is consistent with the behavior of our MoS_2 devices, as shown in the carrier transport behavior in Figure 3a and 3b, where the electron transport is dominant over the entire range of gating voltage (-20 to 60 V). This n-doping effect in the flat MoS_2 also results in a higher conductivity than that of wrinkled MoS_2 (higher resistance in the single-wrinkle device). Instead of one type of resistance (R_F) in a flat-MoS_2 device, MoS_2-wrinkle devices can be modelled as having three resistors in series: $R_W = R_{F1} + R_{WR} + R_{F2}$, where $R_{F1}$and R_{F2} are the resistances of flat regions on the left and right sides of the wrinkle, respectively, and R_{WR} is the resistance of a single wrinkle, as shown in Figure 3e. At 300K, the resistance of a flat-MoS_2 device was measured to be about one-eleventh of the effective resistance of the wrinkled device ($\frac{R_F}{R_W} = \frac{1}{10}$) (measured at $V_{DS} = 1V$). The resistance can be written as: $R = \frac{L}{ne\mu A}$, where L is the length of the MoS_2 sheet between the two electrodes, n is the carrier concentration of the channel, e is the elementary charge, μ is the mobility of the charge carriers, and A is the area of the channel. With a negligible difference between the channel areas, the calculated carrier-mobility in the MoS_2-wrinkle is 3.9 times larger than the carrier-mobility on the flat MoS_2 ($\mu_W \approx x\mu_F = 3.9\ \mu_F$). This yields: $\frac{R_F}{R_W} = \frac{\frac{L_F}{n_F}}{\frac{L_{F1}}{n_F} + \frac{L_{F2}}{n_F} + \frac{L_{WR}}{xn_{WR}}} \approx \frac{1}{10}$ (with $V_{DS} = 1V$and $V_{BG} = 0V$ at 300K). From the experimental data, we obtained $L_F \approx 3\ L_{WR}$; therefore, $n_F \approx\ 50.7\ n_{WR}$ (see detail in supplementary information). The doping concentration in SiO_2 supported MoS_2 is about $n_F = 10^{13}$ cm^{-2},[43–48] which gives the carrier concentration in the suspended part of the MoS_2-wrinkle $n_{WR} \approx 1.97 \times 10^{11}$ cm^{-2}. Since the wrinkled part is suspended in the air without surface induced doping, n_{WR} is expected to smaller,[37] as schematically shown in Figure 3f.

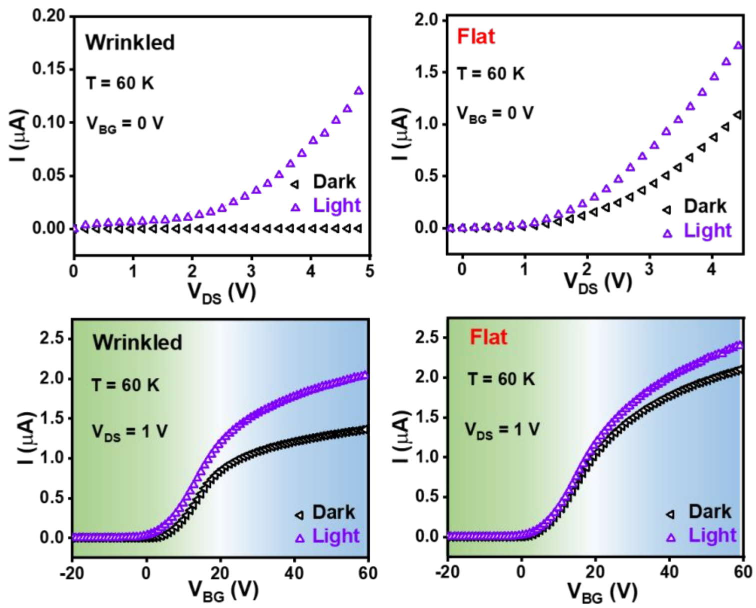

Figure 4. Photo-response studies of single-wrinkle and flat MoS_2 devices. (a) and (b) Photo-response measurements of single-wrinkle and flat MoS_2 devices at 60K, respectively. (c) and (d) Typical source-drain current (I_{DS}) versus back gating voltage (V_{BG}) at 60K for single-wrinkle and flat MoS_2 devices, respectively.

The single wrinkle induced in-plane local strain and doping-redistribution in MoS_2 significantly modifies the photo-response of the MoS_2–wrinkle devices. The photo-response studies were conducted on the both single-wrinkle and flat MoS_2 devices (Figure 4). The photocurrent was slightly higher than dark current (V_{BG} = 0 V) for the flat MoS_2 devices (Figure 4b), which is consistent with previous photo-switching studies in similar conditions.[28] Interestingly, this photo/dark current ratio in wrinkled MoS_2 devices was much higher (Figure 4a). The gate-induced ON/OFF ratio of dark current in flat MoS_2 device (2.9×10^4) (V_{BG} = -20 to 60 V range of back gating) was slightly lower than that of wrinkled MoS_2 device (3.8×10^4) (V_{BG} = -20 to 60 V range of back gating) (Figures 4c and 4d). The photocurrent/dark current ratio at $V_{BG} = 60V$ increases from 1.1 for the flat device to 1.5 for the single-wrinkle device, see in Table S2 in supplementary information. Built-in potential (V_{bi}) induced by the different doping levels in the MoS_2-wrinkle (interfaced region is n-doped from the substrate and the suspended is intrinsic) adds a barrier, thus suppressing the current under small biases. However, at large bias voltage and high positive gate voltage ($V_{DS} \gg V_{bi}$ and $V_{BG} > 10$ V) electrons are expected to tunnel through the depletion region (Zener process). Further, because of the reduced doping, wrinkled MoS_2 exhibits a more semiconducting behavior with considerably higher ON/OFF ratio than substrate-doped n-type flat MoS_2. Under light exposure, the wrinkle-devices exhibited higher gating-induced ON/OFF ratio (2.8×10^3) than flat devices (1.8×10^3) (Figure 4c and 4d). While higher doping density enhances photo-responsivity,[28] in the case of the wrinkle device, the increase in photo-response occurs even with reduced doping.

It should be pointed out that the interactions between light and MoS_2 wrinkle is affected by the shape of the wrinkle, especially the tilted shoulders of wrinkles and nanoscale air gap between the MoS_2 and substrate. The upper surfaces of wrinkled MoS_2 exhibit Fresnel effect, where the wrinkled regions are bright on the ridge and dark on the two shoulders, as shown in Figure S19. The tilted surface of wrinkled MoS_2 cannot induce significant enhancement of absorption of light at wrinkled regions. This is because of relatively small aspect ratio of amplitude/width in wrinkles ($\frac{A}{W} < 0.05$), which keeps the amount of transmitted light on the wrinkle shoulders close to the amount of transmitted light at normal direction (0° angle) on the ridge and flat regions; the details of the calculation are presented in supplementary information. The dark shoulders are attributed to the reduced reflected-light coming back into the camera, as shown in Figure S20 and S21. However, the SiO_2 layer of substrate and the air gap of wrinkled MoS_2 can act as nanocavity and affect the light absorption of MoS_2 flakes. Light interaction with both flat MoS_2 and wrinkled MoS_2 devices are modeled by multilayer structures. The flat sample is treated as a four-layer (Air/MoS_2/ SiO_2/Si) system (Figure S22a) and the wrinkled sample is simplied as a five-layer (Air/MoS_2/Air/ SiO_2/Si) system with delaminated part as a air gap (Figure 5a). With small reflection angles (< 10°), the wrinkles are not expected to have vary in reflectivity. Therefore, the air gap was treated as flat cavities with various heights (0 to 100 nm) with incident angles normal to the air gap. Based on Fresnel equations and optical interference in multilayer thin films[49,50] we calculated the reflection and absorption from the silicon substrate (layer 5) to top-surface air (layer 1). The flat sample can be seem as a special case of wrinkled sample with the thickness of air gap is 0 nm. As shown later, the absorption of MoS_2 ($A_{MoS2} = 0.2901$) with 285 nm SiO_2 in Figure S22a is equal to the absorption of MoS_2 with 0 nm of air gap in Figure 5a. From the Fresnel equations we have:

$$r_{TN} = \frac{r_{N-1N} + r_{TN+1}\exp{(2i\beta_N)}}{1 + r_{N-1N}r_{TN+1}\exp{(2i\beta_N)}} \text{ with (N= 2 or 3)} \quad (5)$$

$$r_{TN} = \frac{r_{N-1N} + r_{NN+1}\exp{(2i\beta_N)}}{1 + r_{N-1N}r_{NN+1}\exp{(2i\beta_N)}} \text{ with (N=4)} \quad (6)$$

Where r_{TN} is the total reflective coefficient from layer N to layer N-1, and N = 2, 3 and 4; $r_{N-1N} = \frac{p_{N-1} - p_N}{p_{N-1} + p_N}$, $p_m = n_m\cos{(\theta_m)}$ *and* $m = 1, 2, 3, 4$ *and* 5; $\beta_N = \frac{2\pi}{\lambda}n_N h_N\cos{(\theta_N)}$ and $\theta_N = sin^{-1}(\sin(\theta_1)/n_N)$. In the calculation $n_1 = 1, n_2 = 4.74 + 1.22i, n_3 = 1, n_4 = 1.5$ *and* $n_5 = 3.9 + 0.025i$, $\theta_1 = 90°$, thickness of MoS_2 $h_2 = 15\,nm$, thickness of SiO_2 $h_4 = 285\,nm$ and wavelength $\lambda = 600\,nm$. The calculations were conductor from the silicon substrate (layer 5) and the total reflection coefficient from silicon layer is $r_{T4} = \frac{r_{34} + r_{45}\exp{(2i\beta_4)}}{1 + r_{34}r_{45}\exp{(2i\beta_4)}}$. r_{T2} and r_{T3} could be obtained in Equation 5. And, reflection $R = \{\text{real}(r_{TN})\}^2 + \{\text{imaginary}(r_{TN})\}^2$ and absorption $A = 1 - R$ were calculated for each layer. The exclusive absorption of MoS_2 layer was collected with each different thickness of air gap (0 to 100 nm), as shown in Figure 5b. For the thin air gap ($h_{air} =$ 0 to 55 nm), the absorption of MoS_2 layer increases from 0.2901($h_{air} =$ 0 nm) to 0.297 ($h_{air} =$ 27 nm) then decreases to 0.2901 ($h_{air} =$ 55 nm). However, a larger thickness air gap ($h_{air} =$ 55 to 100 nm) can reduce the absorption in MoS_2 layer. Therefore, in a wrinkled MoS_2 device with height of 50 nm, the light absorption was enhanced by the nanocavity in the air gap.

The enhancement of photo-response in single-wrinkle devices is attributed to a combination of three events: (a) enhancement of absorption in MoS_2 induced by Fabry-Perot interference in the nanocavity of air gap under the wrinkle, (b) the reduction in the direct transition bandgap enables microscopic funneling of excitons to the wrinkle site (a distortion in the energy band, enabling photo-induced excitons to move to lower bandgap region), and (c) more excitons are focused in a region with a local barrier to transport and with depletion regions enabling increased exciton-separation under external field (or reducing the recombination probability) (Figure 5c to 5e). The fraction of photo-generated electrons that have not recombined in the MoS_2-wrinkle is much larger than that in the flat MoS_2, which leads to more efficient drift of photo-generated electrons. Therefore, much higher photoresponsivity was exhibited by the wrinkled MoS_2. Further, the reduced bandgap provides a wider range of band-transitions for the incident photons; thus enabling a wider energy-range for light absorption. [51]

Futuristically, more significant enhancement is expected to show in multiple wrinkles in series with thinner film thicknesses. The performance of wrinkled device can be enhanced by introducing large bending (aspect ratio $\frac{A}{W}$), which can be achieved by utilizing substrates exhibiting higher surface adhesions with MoS_2. Further, better design of the nanocavity of the air gap under the MoS_2 layer can also improve the performance of MoS_2 devices.

Futuristically, wrinkle device can show more significant enhancement is to have multiple wrinkles in series with thinner film thicknesses. Further, the performance of wrinkled device can be enhanced by introducing large bending (aspect ratio $\frac{A}{W}$), which can be achieved by utilizing substrates exhibiting higher surface adhesions with MoS_2. Better design of the nanocavity of the air gap under the MoS_2 layer can also enhance the performance of MoS_2 devices.

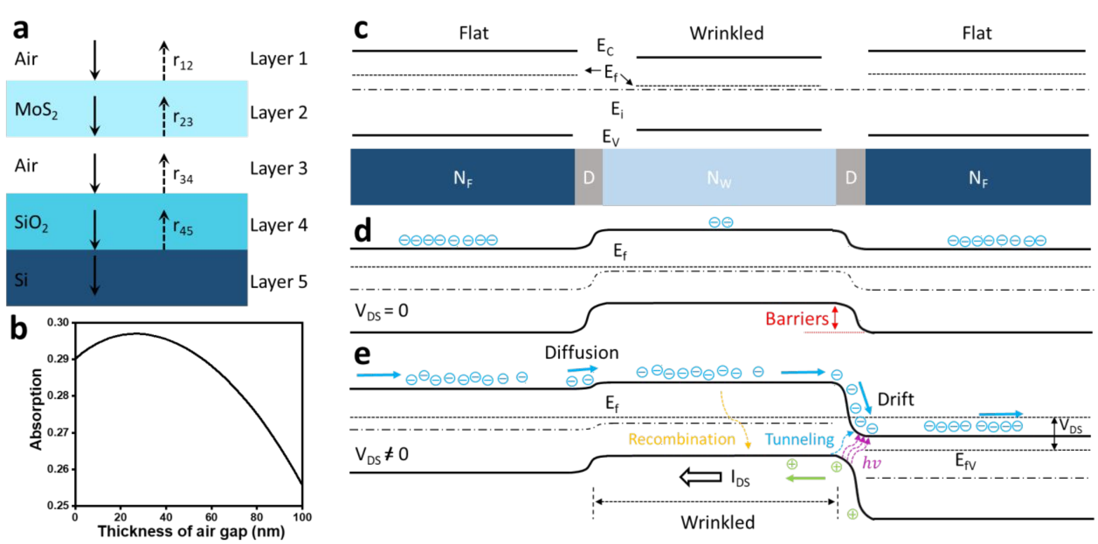

Figure 5. Multilayer interference of the wrinkled device and energy band diagrams of single-wrinkle MoS_2 devices. (a) Schematic Illustration of multilayer model of wrinkled MoS_2 device. (b) absorption of wrinkled MoS_2 at

different thickness of SiO_2. (c) Energy band diagram of individual flat and wrinkled MoS_2; (d) device at no bias; and (e) wrinkled MoS_2 device under bias voltage. Blue and green spheres are electrons and holes, respectively. The filled arrows are the directions of carriers' moving and the unfilled arrows represent the current directions (I_{DS}).

Conclusion

In summary, we show that a single MoS_2 wrinkle can modify the local electronic and optical properties of a MoS_2 device, which can enhance light absorption, enable a control of the transport barrier and the exciton-funneling process towards a confined, low bandgap transition region. Further, the built-in local potential-barrier at the wrinkle site reduces the recombination of excitons under a driving potential which leads to enhanced photo-responsivity. Phonon softening and net mobility enhancement was exhibited by addition of a single wrinkle in a MoS_2 flake. To understand the mechanism of improved photo-responsivity, a comprehensive model was built by combining air gap nanocavity, electronic band-structure, doping density, built-in potential and exciton funneling. This work shows the potential of confined, in-plane structural manipulation of semiconducting 2DNMs and their heterostructures to locally modify the optical transition and in-plane carrier-transport for high functionality, next-generation electronics, optoelectronics, and sensors applications.

Experimental Section

The study was performed on MoS_2 exfoliated on silicon dioxide (285 nm silicon dioxide on silicon) substrates. MoS_2 sheets were cleaved by Scotch tape from the surface of MoS_2 Block (SPI) as shown in Figure 1a. The wafers were diced into about 1×1 cm^2 square pieces, followed by cleaning with acetone and isopropanol, and dried with Nitrogen gas. The tape attached with small flakes of MoS_2 was brought into contact with SiO_2 substrates in dry condition, and a slight pressure was applied for 10s. Then, the tape was quickly peeled off, resulting in MoS_2 deposition on the SiO_2 surface. The van der Waals force between flakes and substrates surface pulled the MoS_2 sheets to have intimate contact with the substrate and separate the attached flakes from the rest of MoS_2 on tape. Therefore, there is no tape residues and tape-induced electrostatic charge at the MoS_2/SiO_2 interface or MoS_2/air interface. During the release of the tape, adhesion between tape and MoS_2 induces partial delamination of MoS_2 from the substrate leading to the bending and wrinkling of

MoS_2. Energy equilibrium between bending energy of single wrinkle and MoS_2/SiO_2 interfacial friction was reached when the MoS_2 contracted to form the wrinkles in MoS_2, as shown in Figure 1b. One in ten time the sheet had wrinkles. The topography of the wrinkles on MoS_2 was characterized by atomic force microscope (AFM) (WiTech Alpha-300-RA) and scanning electron microscopy (FESEM) (Raith). Raman and photoluminescence spectra and position mapping were also collected by WiTech Alpha-300-RA (All the Raman and photoluminescence characterizations were performed at room temperature). For device fabrication, the source and drain regions were defined by laser pattern generator (LW405) followed by electron beam evaporation to deposit 10nm/60nm of Titanium/Gold. The detail of device fabrication process and electrical characterization setup are shown in Figure 3a and Figure S11. The power density of light source in our experiments is 100 $mWcm^{-2}$. Samples are about 10 cm away from the light source.

Conflict of Interest

The authors declare no conflict of interest.

Acknowledgements

This work was supported by the National Science Foundation (Grants: CMMI-1503681 and CMMI-1030963) and University of Illinois at Chicago. We thank Yue Liu for the help with the schematic illustration, and Dr. Sanjay Behura for valuable discussion.

References

1 K. S. Novoselov, D. Jiang, F. Schedin, T. J. Booth, V. V Khotkevich, S. V Morozov and A. K. Geim, *Proc. Natl. Acad. Sci. U. S. A.*, 2005, **102**, 10451–10453.

2 C. Berger, Z. Song, X. Li, X. Wu, N. Brown, C. Naud, D. Mayou, T. Li, J. Hass, A. N. Marchenkov, E. H. Conrad, P. N. First and W. A. de Heer, *Science (80-.).*, 2006, **312**, 1191–1196.

3 S. Bertolazzi, J. Brivio and A. Kis, *ACS Nano*, 2011, **5**, 9703–9709.

4 J. Li, N. V Medhekar and V. B. Shenoy, *J. Phys. Chem. C*, 2013, **117**, 15842–15848.

5 S. Deng, E. Gao, Y. Wang, S. Sen, S. T. Sreenivasan, S. Behura, P. Král, Z. Xu and V. Berry, *ACS Nano*, 2016, **10**, 8403–8412.

6 A. P. M. Barboza, H. Chacham, C. K. Oliveira, T. F. D. Fernandes, E. H. M. Ferreira, B. S. Archanjo, R. J. C. Batista, A. B. de Oliveira and B. R. A. Neves, *Nano Lett.*, 2012, **12**, 2313–2317.

7 A. Castellanos-Gomez, R. Roldán, E. Cappelluti, M. Buscema, F. Guinea, H. S. J. van der Zant and G. A. Steele, *Nano Lett.*, 2013, **13**, 5361–5366.

8 S. Deng and V. Berry, *ACS Appl. Mater. Interfaces*, 2016, **8**, 24956–24961.

9 A. Fasolino, J. H. Los and M. I. Katsnelson, *Nat Mater*, 2007, **6**, 858–861.

10 J. C. Meyer, A. K. Geim, M. I. Katsnelson, K. S. Novoselov, T. J. Booth and S. Roth, *Nature*, 2007, **446**, 60–63.

11 M. J. Cherukara, B. Narayanan, A. Kinaci, K. Sasikumar, S. K. Gray, M. K. Y. Chan and S. K. R. S. Sankaranarayanan, *J. Phys. Chem. Lett.*, 2016, **7**, 3752–3759.

12 V. B. Shenoy, C. D. Reddy, A. Ramasubramaniam and Y. W. Zhang, *Phys. Rev. Lett.*, 2008, **101**, 245501.

13 H. J. Conley, B. Wang, J. I. Ziegler, R. F. Haglund, S. T. Pantelides and K. I. Bolotin, *Nano Lett.*, 2013, **13**, 3626–3630.

14 L. Meng, Y. Su, D. Geng, G. Yu, Y. Liu, R.-F. Dou, J.-C. Nie and L. He, *Appl. Phys. Lett.*, , DOI:http://dx.doi.org/10.1063/1.4857115.

15 V. E. Calado, G. F. Schneider, A. M. M. G. Theulings, C. Dekker and L. M. K. Vandersypen, *Appl. Phys. Lett.*, , DOI:10.1063/1.4751982.

16 J. Zang, S. Ryu, N. Pugno, Q. Wang, Q. Tu, M. J. Buehler and X. Zhao, *Nat Mater*, 2013, **12**, 321–325.

17 J. Quereda, P. San-Jose, V. Parente, L. Vaquero-Garzon, A. J. Molina-Mendoza, N. Agraït, G. Rubio-Bollinger, F. Guinea, R. Roldán and A. Castellanos-Gomez, *Nano Lett.*, 2016, **16**, 2931–2937.

18 N. Liu, Z. Pan, L. Fu, C. Zhang, B. Dai and Z. Liu, *Nano Res.*, 2011, **4**, 996–1004.

19 P. Gerd, C.-G. Andres, B. Michele, S. J. van der Z. Herre, A. S. Gary, K. Agnieszka, H. Thomas, S. Christian and K. Tobias, *2D Mater.*, 2015, **2**, 15006.

20 S. J. Kim, D. W. Kim, J. Lim, S.-Y. Cho, S. O. Kim and H.-T. Jung, *ACS Appl. Mater. Interfaces*, 2016, **8**, 13512–13519.

21 S. Deng and V. Berry, *Mater. Today*, 2016, **19**, 197–212.

22 W. Yan, W.-Y. He, Z.-D. Chu, M. Liu, L. Meng, R.-F. Dou, Y. Zhang, Z. Liu, J.-C. Nie and L. He, *Nat Commun*, , DOI:10.1038/ncomms3159.

23 K. Eun-Ah and A. H. C. Neto, *EPL (Europhysics Lett.*, 2008, **84**, 57007.

24 S. Jung, G. M. Rutter, N. N. Klimov, D. B. Newell, I. Calizo, A. R. Hight-Walker, N. B. Zhitenev and J. A. Stroscio, *Nat Phys*, 2011, **7**, 245–251.

25 A. G. Kvashnin, P. B. Sorokin and B. I. Yakobson, *J. Phys. Chem. Lett.*, 2015, **6**, 2740–2744.

26 S. Deng, A. V Sumant and V. Berry, *Nano Today*, , DOI:https://doi.org/10.1016/j.nantod.2018.07.001.

27 B. Radisavljevic, A. Radenovic, J. Brivio, V. Giacometti and A. Kis, *Nat. Nanotechnol.*, 2011, **6**, 147–150.

28 Z. Yin, H. Li, H. Li, L. Jiang, Y. Shi, Y. Sun, G. Lu, Q. Zhang, X. Chen and H. Zhang, *ACS Nano*, 2012, **6**, 74–80.

29 S. Deng, E. Gao, Z. Xu and V. Berry, *ACS Appl. Mater. Interfaces*, 2017, **9**, 7812–7818.

30 D. Lloyd, X. Liu, J. W. Christopher, L. Cantley, A. Wadehra, B. L. Kim, B. B. Goldberg, A. K. Swan and J. S. Bunch, *Nano Lett.*, 2016, **16**, 5836–5841.

31 C. Rice, R. J. Young, R. Zan, U. Bangert, D. Wolverson, T. Georgiou, R. Jalil and K. S. Novoselov, *Phys. Rev. B*, 2013, **87**, 81307.

32 A. Splendiani, L. Sun, Y. Zhang, T. Li, J. Kim, C.-Y. Chim, G. Galli and F. Wang, *Nano Lett.*, 2010, **10**, 1271–1275.

33 K. F. Mak, C. Lee, J. Hone, J. Shan and T. F. Heinz, *Phys. Rev. Lett.*, 2010, **105**, 136805.

34 S. Mouri, Y. Miyauchi and K. Matsuda, *Nano Lett.*, 2013, **13**, 5944–5948.

35 H.-P. Komsa and A. V Krasheninnikov, *Phys. Rev. B*, 2012, **86**, 241201.

36 J. Feng, X. Qian, C.-W. Huang and J. Li, *Nat Phot.*, 2012, **6**, 866–872.

37 C.-C. Wu, D. Jariwala, V. K. Sangwan, T. J. Marks, M. C. Hersam and L. J. Lauhon, *J. Phys. Chem. Lett.*, 2013, **4**, 2508–2513.

38 D. R. Khanal and J. Wu, *Nano Lett.*, 2007, **7**, 2778–2783.

39 E. Lind, A. I. Persson, L. Samuelson and L.-E. Wernersson, *Nano Lett.*, 2006, **6**, 1842–1846.

40 Y. Ge, W. Wan, W. Feng, D. Xiao and Y. Yao, *Phys. Rev. B*, 2014, **90**, 35414.

41 M. H. and M. E. and M. P. and D. Esseni, *J. Phys. D. Appl. Phys.*, 2015, **48**, 375104.

42 S. Behura, P. Nguyen, S. Che, R. Debbarma and V. Berry, *J. Am. Chem. Soc.*, 2015, **137**, 13060–13065.

43 K. Kaasbjerg, K. S. Thygesen and K. W. Jacobsen, *Phys. Rev. B*, 2012, **85**, 115317.

44 B. Chakraborty, A. Bera, D. V. S. Muthu, S. Bhowmick, U. V Waghmare and A. K. Sood, *Phys. Rev. B*, 2012, **85**, 161403.

45 K. F. Mak, K. He, C. Lee, G. H. Lee, J. Hone, T. F. Heinz and J. Shan, *Nat Mater*, 2013, **12**, 207–211.

46 X. Cui, G.-H. Lee, Y. D. Kim, G. Arefe, P. Y. Huang, C.-H. Lee, D. A. Chenet, X. Zhang, L. Wang, F. Ye, F. Pizzocchero, B. S. Jessen, K. Watanabe, T. Taniguchi, D. A. Muller, T. Low, P. Kim and J. Hone, *Nat Nano*, 2015, **10**, 534–540.

47 B. W. H. Baugher, H. O. H. Churchill, Y. Yang and P. Jarillo-Herrero, *Nano Lett.*, 2013, **13**, 4212–4216.

48 B. Radisavljevic and A. Kis, *Nat Mater*, 2013, **12**, 815–820.

49 C. J. and H. S. and C. Z. and Z. L. and A. L. E. and D. J. and M. T. and Q. G. and Z. Liu, *2D Mater.*, 2016, **3**, 25017.

50 M. A. Kats, R. Blanchard, P. Genevet and F. Capasso, *Nat. Mater.*, 2012, **12**, 20.

51 Q. H. Wang, K. Kalantar-Zadeh, A. Kis, J. N. Coleman and M. S. Strano, *Nat. Nanotechnol.*, 2012, **7**, 699–712.

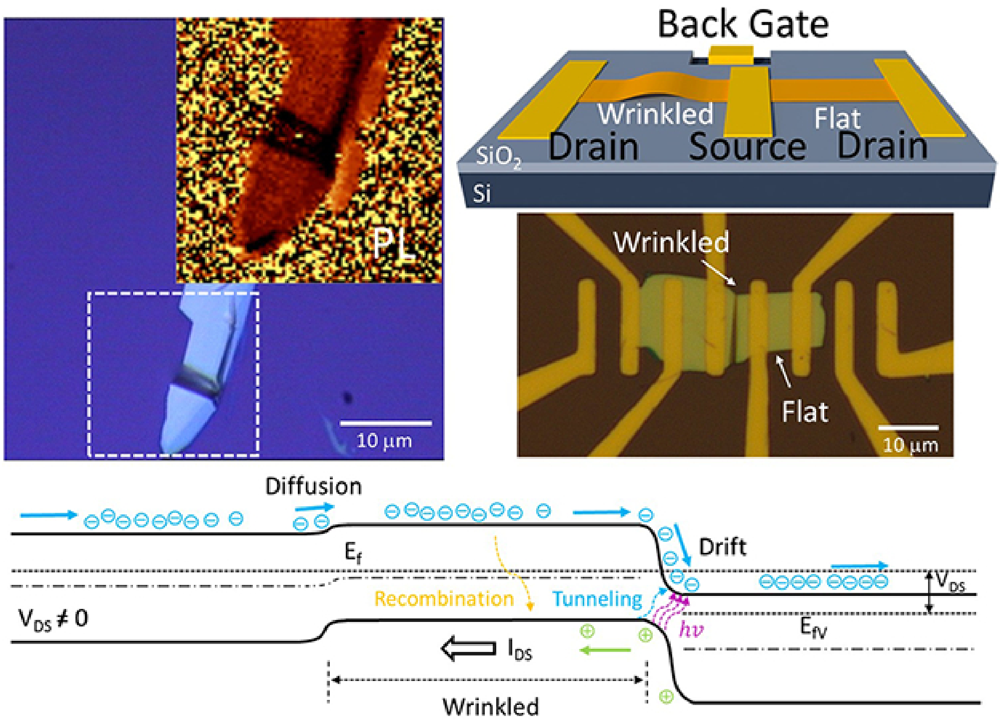
PL
10 μm
Back Gate
Wrinkled
Flat
SiO_2
Drain
Source
Drain
Si
Wrinkled
Flat
10 μm
Diffusion
Drift
E_f
V_{DS}
Recombination
Tunneling
$V_{DS} \neq 0$
hv
E_{fV}
I_{DS}
Wrinkled